Chemical Geology 404 (2015) 27–40

Contents lists available at ScienceDirect

Chemical Geology

journal homepage: www.elsevier.com/locate/chemgeo

Can Mn–S redox cycling drive sedimentary dolomite formation? A hypothesis

Daniel A. Petrash [a,*], Stefan V. Lalonde [b], Gabriela González-Arismendi [a], Robert A. Gordon [c], José A. Méndez [d], Murray K. Gingras [a], Kurt O. Konhauser [a]

[a] Department of Earth and Atmospheric, University of Alberta, Edmonton, Alberta T6G 2E3, Canada
[b] UMR6538 Domaines Océaniques, CNRS-Université de Bretagne Occidentale, Institut Universitaire Européen de la Mer, 29280 Plouzané, France
[c] CLS@APS, Canadian Light Source and Advanced Photon Source Sector 20, Argonne National Laboratory, IL 60439, USA
[d] Instituto de Ciencias de la Tierra, Universidad Central de Venezuela, Caracas, Venezuela

ARTICLE INFO

Article history:
Received 14 September 2013
Received in revised form 12 March 2015
Accepted 16 March 2015
Available online 25 March 2015

Editor: Michael E. Böttcher

Keywords:
Mn-cycling
Peritidal dolomite
Synsedimentary dolomite
Microbial mats
Shallow burial diagenesis

ABSTRACT

The formation of dolomite in modern peritidal environments is linked to the degradation of buried microbial mats, with complexation of Ca and Mg by extracellular polymeric substances (EPSs) and alkalinity generation through organic carbon respiration facilitating the nucleation of dolomite precursors. In the past two decades, microbial sulfate reduction, methanogenesis, and methanotrophy have all been considered as potential drivers of the nucleation process, but it remains unclear why dolomite formation could not also occur in suboxic sediments where abundant alkalinity is produced by processes linked to Mn(IV) and/or Fe(III) reduction coupled with the diffusion and reoxidation of reduced sulfur species. Here we report the interstitial occurrence of spheroidal aggregates of nanometer-scale Ca-rich dolomite rhombohedra within suboxic sediments associated with remnant microbial mats that developed in the peritidal zone of the Archipelago Los Roques, Venezuela. Multiple analytical tools, including EPMA, ICP-MS, synchrotron-based XRF and XRD, and spatially resolved XANES microanalyses, show that the dolomite-cemented interval exhibits depleted bulk iron concentrations, but is interstitially enriched in Mn and elemental sulfur (S^0). Manganese occurs in several oxidation states, indicating that the dolomite-cemented interval was the locus of complex biological redox transformations characterized by coupled Mn and S cycling. The tight correspondence between sedimentary Mn and $MgCO_3$ concentrations further hints at a direct role for Mn during dolomitization. While additional studies are required to confirm its relevance in natural settings, we propose a model by which coupled Mn–S redox cycling may promote alkalinity generation and thus dolomite formation in manner similar to, or even more efficiently, than bacterial sulfate reduction alone.

1. Introduction

In the peritidal zone of most Holocene carbonate platforms, Ca-dolomite formation has been linked to the near-surface decay of microbial mats (e.g., Kendall and Skipwith, 1968; Gebelein and Hoffman, 1973; Davies et al., 1975; Von der Borch and Lock, 1979) that were rapidly buried during sediment progradation (Hardie and Shinn, 1986). While modern hypersaline microbial mats are functionally diverse (Des Marais, 2003), their upper trophic structure is generally composed of halophilic cyanobacteria living in close association with halotolerant algae and other oxygenic and anoxygenic autotrophs, while the deeper levels contain various heterotrophic communities which couple the oxidation of buried organic carbon to the reduction of available terminal electron acceptors (TEAs). These TEAs include (in decreasing order of energy yield), oxygen, nitrate, manganese, iron, sulfate, and ultimately dissolved inorganic carbon (Froelich et al., 1979). The progressive depletion of TEAs often leads to sharp biogeochemical interfaces that may favor the precipitation of authigenic minerals, such as calcite, phosphates, pyrite and/or dolomite (see Konhauser, 2007).

The fact that dolomite is abundant in the geologic record yet is rarely observed forming today (the so-called "dolomite problem") is complicated by the fact that Mg in seawater today is largely found in complexed form (cf. Arvidson and MacKenzie, 1999). In the limited number of modern dolomite-forming systems known today, this is thought to be overcome in several ways. The extracellular polymeric substances (EPSs) produced by benthic microbes facilitate the sorption and accumulation of Ca, Mg, and various trace metals, and may also act as a mineral nucleation template (Défarge et al., 1996; Braissant et al., 2007, 2009; Wang et al., 2009). Recent work by Roberts et al. (2013) details how the variety of carboxylated macromolecules comprising EPSs may catalyze the precipitation of dolomite through complexation and dehydration of Mg^{2+} ions (see also Kenward et al., 2013). The anaerobic respiration of organic carbon shifts the pH towards alkaline values and

* Corresponding author.
E-mail address: petrash@ualberta.ca (D.A. Petrash).

http://dx.doi.org/10.1016/j.chemgeo.2015.03.017
0009-2541/

increases the activity of CO_3^{2-} ions, both favoring dolomite saturation by displacing water dipoles bonded to the surface of magnesium cations (Lippmann, 1973; Slaughter and Hill, 1991; Défarge et al., 1996; Castanier et al., 1999; Raz et al., 2000; Decho et al., 2005; Gilbert et al., 2005; Kwak et al., 2005; Visscher and Stolz, 2005; Braissant et al., 2007; Wang et al., 2009; Gallagher et al., 2012). It is by this combination of biologically-influenced (i.e., ion adsorption and mineral templating) and biologically-induced (metabolically-controlled) mechanisms (cf. Dupraz et al., 2009) that points to many heterotrophic bacteria being capable of facilitating Ca-dolomite nucleation. Yet, the anaerobic respiratory pathway that has received the most attention in terms of diagenetic carbonate mineral formation is bacterial sulfate reduction (Vasconcelos et al., 1995; Vasconcelos and McKenzie, 1997; Wright, 1999; Wright and Wacey, 2005; Warthmann et al., 2000; Van Lith et al., 2003; Sánchez-Román et al., 2009). While studying dolomite formation in hypersaline mats from Lagoa Vermelha, Brazil, Moreira et al. (2004) concluded that the mineral actually forms as a result of undersaturation of competing carbonate phases due to sulfide oxidation. Similarly, it has been proposed that sulfide ions or some organic ligands may promote Mg^{2+} dehydration at the surface of a solid precursor phase resulting in dolomite nucleation/precipitation reactions (Zhang et al., 2012; Yang et al., 2012, see also Roberts et al., 2013).

It is thus apparent that a variety of mechanisms, non-exclusive in nature, can act as potential promoters of dolomite formation. In some marine sediments, the activity of subsurface Mn(IV)- and Fe(III)-reducing bacteria exerts a quantitatively important control over rates of organic carbon mineralization (Aller and Rude, 1988; Aller, 1990, 1994; Canfield et al., 1993a,b; Thamdrup et al., 1994), and not surprisingly, these microorganisms have also been found potentially associated with dolomite precipitation (see for instance Compton, 1992; Curtis et al., 2000; Breuker et al., 2013). However, sedimentary evidence for links between metal respiration during suboxic diagenesis and dolomite formation has yet to be reported.

In this study we employ a high resolution chemostratigraphic approach, complemented by synchrotron-based microscale analyses and microbial surface chemical characterization (potentiometric and FTIR), with the goal of examining the formation of dolomite in association with buried microbial mats of hypersaline lagoonal sediments in the Archipelago Los Roques, Venezuela, and specifically the potential role of electron acceptors other than sulfate in the dolomitization process. We describe a surprising relation between the subsurface availability of manganese and the abundance of dolomite at this site, where it appears that progressive degradation of a rapidly buried microbial mat system produced a geochemical disequilibrium zone marked by the availability, and recycling, of intermediate manganese and sulfur species. We propose a reaction model whereby intermediate Mn(III) phases, formed via Mn(IV) reduction or Mn(II) oxidation, reacted with native and evolved S^0, enhanced the degradation of sedimentary organic matter, sustained favorable alkalinity and pH, and ultimately, contributed to the stabilization (i.e., progressive growth) of early formed dolomite precursors as microcrystalline Ca-dolomite cements.

2. Study site

Francisqui is one of the many cays comprising the Archipelago Los Roques, an arid isolated carbonate platform located 150 km from the Venezuelan coastline in the Caribbean Sea (see Fig. 1A). The platform developed over an uplifted lithospheric block whose age, petrography, geochemistry, and tectono-magmatic history are similar to exposures of the Caribbean Plate on the nearby Leeward Antilles islands (see Wright and Wyld, 2011). The restricted lagoon sampled (Fig. 1B) has an areal extent of about 7100 m^2; it is shallow (average water depth < 15 cm), alkaline (pH = 9.3; $CaCO_{3\ total}$ = 259 meq/L) — as determined in the field, and hypersaline (salinity = 138–141‰) — as determined in the lab (using measured Cl^- concentrations). Other relevant chemical features of the lagoon water are summarized in Tables 1 and 2, and its predicted saturation states with regard to a variety of minerals are shown in Table 2. The lagoon has been infilled by accretion of sediments of both authigenic and allogenic (storm transported) origin (i.e., Hardie and Shinn, 1986). A subaqueous microbial mat, composed of both photosynthetic and non-photosynthetic microbes, has developed across the lagoon due to the suppression of most grazing activity under the hypersaline conditions governing this environment (Fig. 1C–D). The organic-rich mud-dominated lagoonal succession reflects annual low amplitude fluctuations of the lagoon water level (Fig. 1C). The range of such oscillations is controlled by seepage reflux, and sporadically by storm events. The sedimentary distribution of organic matter is greatly influenced by such autocyclic controls, and fossil analogues to the surficial mat have been buried due to active sediment accumulation.

3. Methods

With the goal of investigating the formation of dolomite in association with the oxidation of the buried microbial mats and the potential role of electron acceptors other than sulfate, we combined information obtained via bulk sediment digestion and Inductively Coupled Plasma-Quadrupole Mass Spectrometry (ICP-QMS) with a range of textural, mineralogical and in situ geochemical analyses. We also evaluated the reactivity of the surficial microbial mats by potentiometric titration and applied a surface complexation model that benefits from complimentary Fourier Transform Infrared Spectroscopy (FTIR) data.

3.1. Sample collection

A Glew Gravity Corer (Glew, 1991) was used to collect 30 cm-long vertical cores of lagoon sediments. The cores were then extruded and sliced into 0.5 cm subsamples, for the first 6 cm, and then into 2 cm subsamples for the deeper part of the core. Sub-samples of the organic rich sediments were placed in sterile 0.5 mL Eppendorf PCR polypropylene tubes containing filtered lagoon water and aqueous glutaraldehyde to a final concentration of 2% v/v. The overlying surface waters were sampled in duplicate and filtered through Spectra micropore 0.22-μm filters. One of the aliquots was immediately acidified with concentrated trace metal-free HNO_3 for cation analyses, and the other left unacidified for anion analysis. The sediment subsamples were freeze-dried prior to further analyses. The samples were kept refrigerated (3 °C) prior to all sample preparation and analyses.

3.2. Bulk mineralogical analysis

The mineralogy of freeze-dried bulk sediments (0–30 cm depth) was determined at a vertical resolution of 2 cm by X-ray Diffraction (XRD), with patterns produced using a Rigaku Geigerflex Power Diffractometer with Co-Kα radiation generated at 50 kV and 25 mA, a step size of 0.5° $2\theta \cdot step^{-1}$, and an accumulation time of 2 $s \cdot step^{-1}$. In the samples where dolomite was found, we optimized the XRD in the interval 29 to 38° 2θ using the d_{101} peak of quartz for calibration purposes. The refined XRD patterns were obtained at 0.2° $2\theta \cdot min^{-1}$, and a step size of 0.004° $2\theta \cdot step^{-1}$ (after Jones et al., 2001).

3.3. Electron microscopy

Scanning Electron Microscopy (SEM) observations of both the surface microbial mat and the dolomite-bearing sediments were performed on a JEOL JSM-6301FXV instrument connected to a Norvar Energy-Dispersive Spectrometer (EDS). Freshly broken samples were graphite coated for SEM observation, while others were cryosectioned and observed by Transmission Electron Microscopy (TEM). The SEM analyses were done at accelerating voltages of 5 kV (20 kV for EDS), and at a working distance of 11 mm. The accelerating voltage of TEM was 80 kV (see Petrash et al., 2012 for further details).

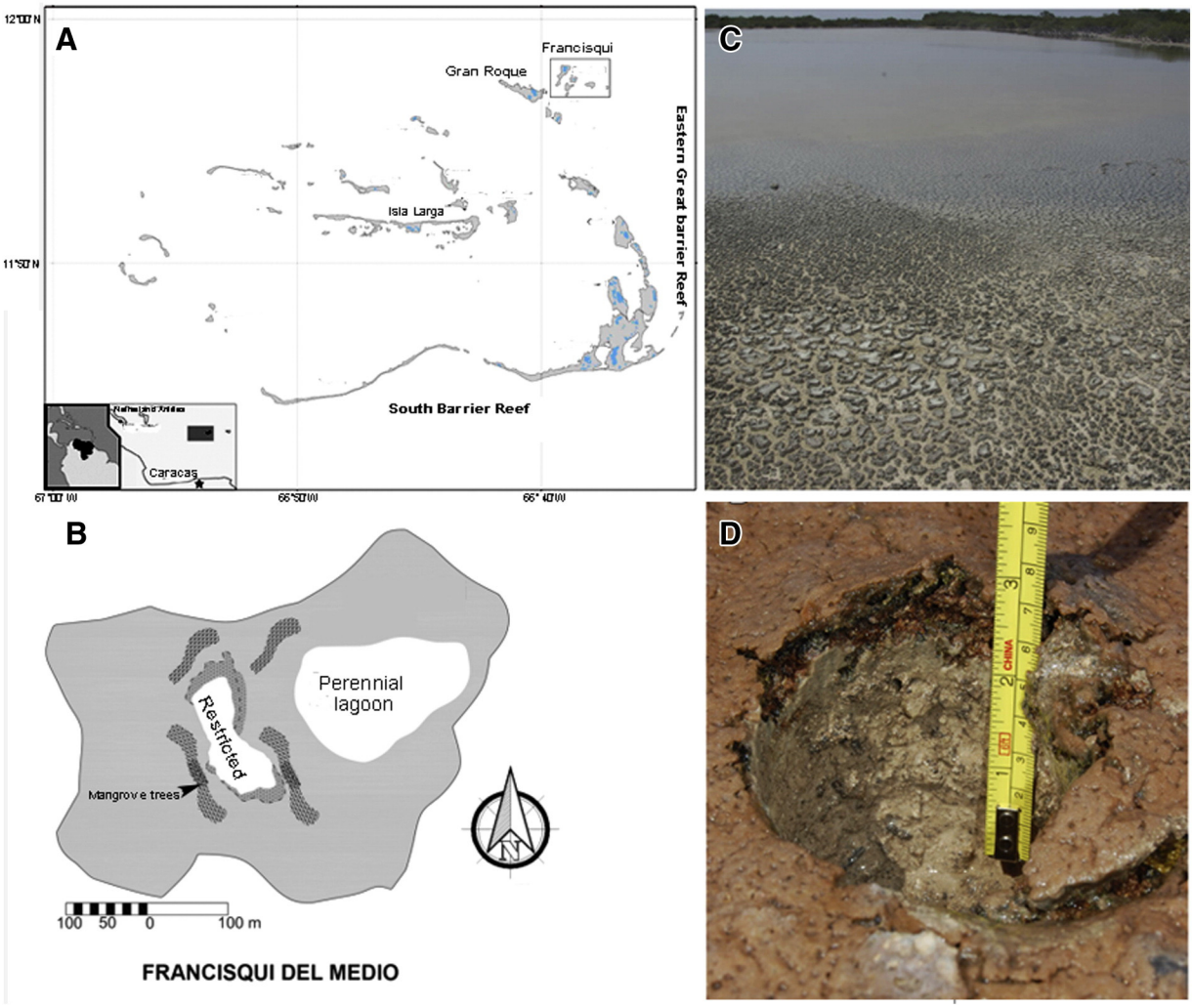

Fig. 1. Archipiélago Los Roques National Park, Venezuela. A: The Archipelago consists of more than 42 cays, most of them exhibiting at least one restricted lagoon. B: The selected study site is the hypersaline lagoon Francisqui del Medio. C: Desiccated microbial mats remain as evidence of seasonal variations in the lagoonal water level. D: The communities comprising these mats produce copious amounts of exopolymers.

3.4. Solid phase geochemistry

Samples were freeze dried and powdered before analysis. For minor and trace element composition, a mass of ~200 mg of each sediment subsample was digested using analytical grade HNO_3 (8 N) to ensure dissolution of all but the most refractory detrital grains. The transition metal concentrations were determined by ICP-QMS using a PerkinElmer Elan 6000 instrument. The Total Organic Carbon (TOC) and Total Nitrogen (TN) of sediment subsamples were determined using the Dumas Combustion Method in a Costech 4010 Elemental Analyzer. We complemented our bulk ICP-QMS analyses with laser ablation (LA) ICP-QMS (28 laser spots) in order to measure Mg, Mn, Fe, and Sr concentrations of the sediments comprising the interval from 8 to 14 cm depth, where Ca-dolomite was identified via XRD. Ca-concentrations, obtained via WDX (see below), were used as internal standards and the USGS analytical standard MACS-3 was used to derive the trace metal concentrations of the samples. Measuring conditions and detection limits are as described in Petrash et al. (2012).

3.4.1. Sorptive properties of the microbial mats and their influence on sediments

In order to evaluate the sorptive properties of individual layers comprising the microbial mat, 500 mg (dry weight) sub-samples of the green (upper) and purple (lower) layers of the mat at the sediment–water interface were examined by potentiometric acid–base titration. Samples were first washed with four alternating wash and harvest cycles (10-s agitation followed by 10-min soak and centrifugation at 11,050 g) at circumneutral pH with ultra-pure (18.2 MΩ) water in order to replace interstitial waters and release surface-complexed elements (e.g., Lalonde et al., 2007). Samples were then suspended in ~40 mL of 0.01 M $NaNO_3$ titration electrolyte and adjusted to pH ~3 with concentrated analytical grade HNO_3. Sub-samples were titrated up from pH ~3 to pH 11 and a surface complexation model was fitted to the resulting excess charge data following the methods of Lalonde et al. (2007, 2010). Briefly, the set of functional groups (in terms of concentrations and proton stability constants) that best account for the excess charge data for each titration were determined by linear programming over a fixed grid of possible pK_a values (in this case, 4–10 in 0.2 increments). We also conducted synchrotron-based FTIR using a Ge IR attachment for attenuated total internal reflection. These analyses were conducted at the Mid IR Beamline (01B1-1) at the Canadian Light Source, and provide identification of the organic ligands contributing to the surface reactivity of the surficial microbial mat with high spatial resolution and minimum sample preparation.

To evaluate the extent to which biologically important metals are transferred from ambient waters to the surficial microbial mats and subsurface sediments, we examined Ca-normalized distribution

Table 1
Lagoon water and bulk-sediment trace element concentrations. Grey shadowed zone represents the living microbial mat, values in bold are the Ca-dolomite cemented interval of buried microbial mat. See also Supplementary Table 1.

Analyte	Ti	V	Cr	Mn	Fe	Co	Ni	Cu	Zn	Mo
$[Me]_{lw}$	2.95	4.87	0.32	1.25	1.64	0.12	0.50	18.41	1.24	1.63
Depth	Ti	V	Cr	Mn	Fe	Co	Ni	Cu	Zn	Mo
0.25	159.9	43.3	41.6	140.1	6179.2	13.4	202.3	39.3	81.23	52.0
0.75	82.7	27.4	25.3	106.9	4654.6	1.4	<D.L.	45.2	74.49	48.2
1.25	78.0	26.8	22.6	94.8	4253.4	1.1	<D.L.	46.6	102.32	69.5
1.75	169.6	66.1	45.0	189.1	7331.7	1.7	<D.L.	122.1	203.37	155.9
2.25	159.5	36.7	29.0	124.9	5044.4	0.7	<D.L.	60.9	113.50	91.3
2.75	117.5	45.6	31.4	151.7	5507.4	1.1	<D.L.	80.7	153.90	105.5
3.25	131.0	51.9	40.1	174.0	6163.6	1.8	<D.L.	107.2	177.66	150.3
3.75	92.4	35.7	26.7	148.7	4231.9	0.5	<D.L.	63.8	129.57	88.8
4.25	87.2	34.6	26.2	145.6	4041.8	0.6	<D.L.	74.3	143.91	92.5
4.75	69.5	25.1	21.5	137.8	3056.2	<D.L.	<D.L.	50.4	99.89	60.8
5.25	76.9	25.3	22.0	136.5	3056.2	<D.L.	<D.L.	50.0	101.35	59.7
5.75	87.5	20.9	17.9	125.1	2692.3	<D.L.	<D.L.	39.1	118.33	107.4
7	127.4	32.8	29.3	178.8	3613.5	<D.L.	<D.L.	61.3	150.15	24.3
9	109.9	28.6	36.0	260.4	2090.9	2.1	<D.L.	20.0	179.73	27.1
11	129.6	39.3	39.9	252.3	2207.0	3.3	5.5	27.7	195.53	57.7
13	123.2	35.1	49.7	280.7	2409.7	4.7	32.1	29.0	219.64	70.3
15	630.3	58.3	70.9	155.0	1940.4	5.7	59.6	49.4	569.28	47.7
17	452.1	50.7	70.9	119.2	1940.2	6.8	79.3	39.2	346.77	15.2
19	165.0	50.4	69.5	73.3	1714.7	8.5	115.3	24.6	172.28	11.5
21	196.2	62.8	74.9	68.2	2255.8	10.3	147.5	24.3	155.66	10.3
23	206.6	87.5	88.2	76.8	2615.2	11.4	174.8	30.9	167.64	11.5
25	239.3	89.2	89.5	79.3	2697.7	13.3	200.0	31.3	165.94	7.0
27	191.2	89.0	80.0	68.1	2102.6	11.3	180.9	26.6	152.11	7.3
29	117.1	101.6	70.6	56.9	1686.6	12.1	204.0	18.8	94.51	15.2
SE	7.9	0.6	0.5	1.8	18.9	0.7	9.4	0.7	1.4	0.4

Concentrations are given in nmol·(g dry wt.)$^{-1}$, except for $[Me]_{lw}$ (concentrations measured in the surficial lagoon water) which are in nM; SE: measured standard error (based in 3 replicates).

coefficients between lagoon water ($[Me]_{lw}$ / $[Ca]_{lw}$) and bulk sediments ($[Me]_{Sed}$ / $[Ca]_{Sed}$). In the context of the uppermost mat layer, this approach provides an indication of the affinity of the mat for certain biologically important metals, and variation down core reveal shifts in the mobility of these elements upon burial and diagenesis. Elemental distribution coefficients for the mat and underlying sediments were calculated using the relation:

$$D_{Me} = ([Me]_{Sed}/[Me]_{lw}) \cdot ([Ca]_{lw}/[Ca]_{Sed}).$$

3.4.2. Statistical characterization of the sedimentary chemofacies

A Spearman rank correlation coefficient (r_s, $p < 0.001$) was used as a non-parametric measure of the strength and direction of association between any two parameters of interest. Geochemical behavior and correlation amongst elements throughout the sedimentary pile (fraction soluble in 8 M HNO_3, thus excluding refractory detrital minerals) were further examined by hierarchal cluster analysis, which offers a secondary and objective test of the elemental grouping in each diagenetic zone. The data standardization and clustering protocols implemented here (Filzmoser and Hron, 2008; Montero-Serrano et al., 2010) emphasize the relative similarity between analytes by means of squared normalized Euclidian distances. The analyses were performed using the Multi-Variate Statistical Package R.

3.5. Aqueous geochemistry

Overlying water temperatures and pH values were measured immediately upon collection using a Ross (Orion) combination pH electrode and salinity-matched buffers, and pH values are reported on the operational scale (Covington and Whitfield, 1988). Alkalinity was measured in situ by acid titration and a mixed pH indicator. Results are expressed as calcium carbonate ($CaCO_3$). Quantitative analyses of SO_4^{2-} and Cl^- anions in the surficial lagoon water samples were performed using a Dionex DX600 Ion Chromatograph. We derive salinity (S) from chlorine concentrations by using the empirical relationship S (‰) = 1.80655 [Cl^-]. Filtered and non-acidified samples were diluted as required before analysis to reduce salinity to operational values adequate for the analytical machine. Field measurements of temperature, pH, dissolved oxygen and alkalinity, and the chemical analyses of the water samples were used as input data to calculate the distribution of aqueous species, ion activities, and mineral saturation indices that indicate the tendency of a water to dissolve or precipitate relevant mineral phases (see Drever, 1988). The model was computed using the chemical speciation code WATEQ4F (Ball and Nordstrom, 1991) as implemented in PHREEQC

Table 2
Activity of dissolved species and saturation indexes (SI) of predicted mineral phases ($\Omega > 0$) in the surficial lagoon water as determined using the chemical speciation code WATEQ4F as implemented in PHREEQC (Parkhurst and Appelo, 1999).

Phase		SI	Log IAP	Log KT
Goethite	FeOOH	7.0	5.7	−4.7
Huntite	$CaMg_3(CO_3)_4$	5.8	−24.7	2.7
Maghemite	Fe_2O_3	5.0	11.3	−9.0
Dolomite(d)	$CaMg(CO_3)_2$	4.0	−12.8	−3.0
Hydromagnesite	$Mg_5(CO_3)_4(OH)_2 \cdot 4H_2O$	3.5	−6.4	−30.5
Artinite	$MgCO_3 \cdot Mg(OH)_2 \cdot 3H_2O$	2.6	11.6	6.4
Magnesite	$MgCO_3$	2.2	−6.0	−17.3
Calcite	$CaCO_3$	1.8	−6.8	9.0
Aragonite	$CaCO_3$	1.6	−6.8	−8.2
Brucite	$Mg(OH)_2$	1.4	17.6	6.9
Hausmannite	Mn_3O_4	1.3	60.1	7.3
$Fe(OH)_3$(a)	$Fe(OH)_3$	0.7	5.6	−8.4
Strontianite	$SrCO_3$	0.3	−9.0	16.3
Gypsum	$CaSO_4 \cdot 2H_2O$	0.3	−4.3	58.9
Celestite	$SrSO_4$	0.2	−6.5	8.3
Bixbyite	Mn_2O_3	0.04	−0.9	−6.7

Activity of dissolved species and saturation indexes (SI) of predicted mineral phases in the surficial lagoon waters. SI = log (IAP / Ksp), with IAP and Ksp being the ion activity product of the dissolved constituents and solubility product, respectively. Calculation were performed using the following parameters: Salinity = 140‰; pH = 9.3; $CaCO_{3(Tot)}$ = 259 meq/L; $[Cl^-]$ = 77,260 mg/L, $[SO_4^=]$ = 13,269 mg/L; Mg/Ca = 6.1, with dissolved concentrations of [Ca] = 1370; and [Sr] = 274; [Fe] = $9.16 \cdot 10^{-2}$, [Mn] = $6.9 \cdot 10^{-3}$, [Zn] = $7.33 \cdot 10^{-2}$, [Cu] = 1.16 ppm.

(Parkhurst and Appelo, 1999), and assumes homogeneous aqueous phase equilibria, except for redox species. The thermodynamic database used is Nordstrom et al. (1990), revised by Ball and Nordstrom (1991) for gypsum. Equilibrium with respect to mineral solubilities is not assumed. The program results are used primarily to place constraints on potential mineral precipitation reactions at the sediment–water interface. For determination of major and trace metal compositions of the lagoon water, the samples were digested with HNO_3 (8 N) and analyzed according to standard procedures (e.g., Windom et al., 1989) using the quadrupole ICP-MS instrument described above.

3.6. Electron Probe microanalyses (EPMA)

The in situ distributions and concentrations of major elements Ca, Mg, Mn, S, and P in sediments comprising the dolomite-bearing zone were determined using Wavelength Dispersive X-ray Spectroscopy (WDS) with a JEOL JXA-8900 electron microprobe operated at an accelerating voltage of 15 kV, focused beam diameter of 40 μm ($A \approx 1256.6\ \mu m^2$), and an average current of 10 nA. Count times were 20 s on each peak and half that for background measurements; detection limits (3σ) from the average of three analyses were approximately 250 ppm for most of the analyzed oxides. A combination of natural and synthetic mineral, oxide, and metal standards was used to reduce counts to weight percent concentrations using the CITZAF method with φρZ calculation.

3.7. Synchrotron-based microanalyses

All synchrotron-based elemental microanalyses were conducted under high-resolution conditions by tuning the excitation energy to desired levels using a Si (111) double-crystal monochromator installed at beamline 20 ID at the Advanced Photon Source (APS) in Argonne, IL.

3.7.1. Micro X-ray fluorescence (μ-XRF)

The in situ distributions and concentrations of Mn, Fe, Co, Ni, Zn, and Sr in the dolomite-bearing sediment layer were determined via hard X-ray microprobe analyses. The excitation energy was tuned at 20.196 keV and a flux of 10^{10} to 10^{11} photons-per-second micro-focused over an analytical area of ~30 μm^2 using Kirkpatrick–Baez (KB) mirrors. The resulting fluorescence spectra were measured using a 4 element Vortex multi-element Si drift detector located at 90° to the incident beam in the direction of the polarization. The detector was calibrated to have 30 eV per channel. Semi-quantitative μ-XRF results were obtained via calibration of relative element sensitivities against a chemically homogeneous zone of the USGS MACS-3 reference material. Spectral acquisition involved counting for 60 s. Net intensities of the fluorescence peaks were determined by fitting the complete emission line series of each spectrum in the computer code PyMca v.4.6.2 (Solé et al., 2007).

3.7.2. μ-XANES and μ-XRD

We used μ-XANES for determining the oxidation state and coordination chemistry of Mn in the micritic cements. The pre-edge features were collected in the energy range 6.450–6.690 keV; the main edge crest was collected with 0.50 eV steps, then with 0.05 $Å^{-1}$ steps (in *k*-space) until 200 eV above the absorption edge. XANES results were aligned using the K-edge of a Mn foil standard measured in parallel with the sample (i.e., Kraft et al., 1996) with no energy shifts between scans observed for the simultaneously-measured Mn foil reference. Nine individual Mn K-edge XANES scans were averaged in energy before background removal and normalization to unit edge-step using ATHENA (Ravel and Newville, 2005). Semi-quantitative analysis of these bulk merged Mn K-edge XANES spectra was done through a linear combination-least squares fitting using four model compounds: Mn_2O_3, $MnCO_3$, -MnOOH, and Mn_3O_4. At the end of spectral data collection, the mineralogy of the microanalytical area subjected to XANES was evaluated by integrating its bulk 2D-XRD reflection patterns, produced via a KB micro-focused beam (λ = 0.6139 Å), using the computer code FIT2D (Hammersley et al., 1996). Correction of the experimental geometry and 2θ calibration was made possible by also measuring the reflection patterns of LaB_6.

4. Results and discussion

4.1. Sorptive properties of the living microbial mat

Concentrations and acidity constant (pK_a) values of proton-binding sites modelled from acid–base titration data reveal very little difference between the upper (green) and lower (purple) layers comprising the living microbial mat (Fig. 2A). The total site density in the surficial microbial mat was found to be 3.10 ± 0.63 $mol \cdot kg^{-1}$ (dry). The pK_a distribution of chemical functional groups (Fig. 2A) shows three buffering zones that we attribute to carboxyl groups (apparent pK_a at 4.03 ± 0.32), the combined buffering capacity of phosphoryl and thiol groups (apparent pK_a at 6.2 ± 0.85), and amino groups (apparent pK_a at 9.32 ± 0.60) (see Fein et al., 1997; Braissant et al., 2007). A contribution from thiol functional groups is not only supported by the significant accumulation of intra- and extracellular-sulfur in these mats (see Fig. 2B), but also by the FTIR spectral data (Fig. 2C) that shows peaks at 2550–2620 cm^{-1} which are characteristic of S–H stretching. While more acidic carboxyl, phosphoryl, and thiol groups are more commonly implicated as the primary sites responsible for metal sorption (e.g., Boyanov et al., 2003; Lalonde et al., 2010), the concentration of the third site (amino groups) was found to exceed the combined concentration of the first and second buffering zones (Fig. 2A). This has been previously reported for bacterial cultures producing copious amounts of EPSs (Lalonde et al., 2005; Braissant et al., 2007), and is consistent with visual and TEM observations (Fig. 2D) affirming the EPS-rich nature of the living microbial mat in this study.

At the pH of the lagoon water (pH 9.3) most of the reactive sites identified here will be in a deprotonated state (see Fig. 2A) and available to bind dissolved metal cations (Geesey and Jang, 1989; Decho, 2000). The natural abundance and activity of these cations in the alkaline lagoon water, together with competition based on their ionic radii, charge, and specific organic and inorganic ligand-metal binding constants (Fraústo da Silva and Williams, 2001), determine which metals are preferentially

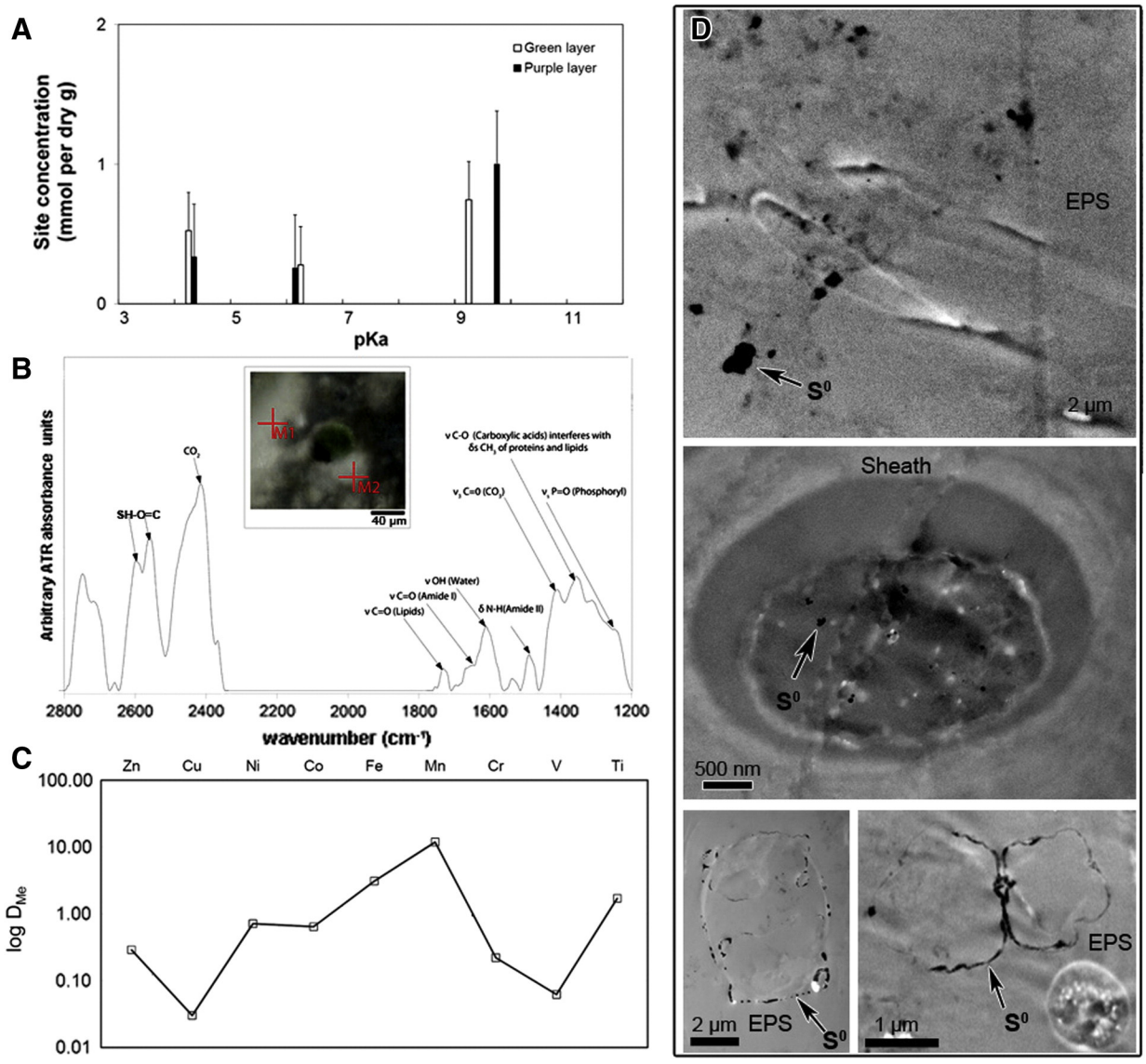

Fig. 2. Reactivity of the surficial microbial mat. Organic functional groups comprising the microbial biomass confer it with a strong capacity for metal sorption. A: Functional group distribution modelled from titration data for upper (green) and lower (purple) photosynthetic mat layers from the hypersaline lagoon in Francisqui. The model represents the set of functional groups, fitted in terms of concentration (y-axis, normalized to dry weight) over a fixed grid of possible acidity constants (x-axis, in this case from 3 to 11 in 0.2 pK_a increments), that best describes the charge excess data over three titration replicates. B: SR-FTIR-ATR spectrum of microbial biomass. C: Logarithmic plot showing enrichment/depletion factors ($D_{Me} = ([Me]_{Sed} / [Me]_{lw}) \cdot ([Ca]_{lw} / [Ca]_{Sed})$) for the first row transition metals in the sediments and surface mat relative to lagoon waters. D: Transmitted electron micrographs of filamentous and coccoid microorganisms associated with S^0-rich mats. Note extracellular, intracellular and cytoplasmic membrane sulfur inclusions, as determined by EPMA.

sequestered by the microbial mat surface (see Table 1, Fig. 2D). Based solely on the total concentration of reactive sites determined for the surficial mat biomass, we calculate that the burial of an equivalent ~2 cm-thick microbial mat (estimated $\rho = 1.15$ kg/m^3) could sequester and transport between 59 and 86 mmol m^{-2} of alkali and transition metals to the subsurface.

4.2. High resolution chemostratigraphy

Solid phase geochemical data reflects exchange and equilibrium between reactive solid phases and pore fluids. The elemental distribution coefficients in the sediments, D_{Me}, reveal three distinct biogeochemical zones, or chemofacies (Fig. 3). These reflect the variable redox behaviour down core of transition metals (e.g., Mn, Ni, Co, and Fe) which form highly insoluble oxides in oxic pore waters, and elements (e.g., Mo and Re) which occur as highly soluble anionic species in oxic and suboxic waters and are rendered insoluble under more reducing conditions where they co-precipitate with sulfides (Tribovillard et al., 2006). These general patterns of metal distribution are also evident in a dendrogram (Fig. 4).

4.2.1. Chemofacies I

From the water–sediment interface downwards to about 6 cm depth is an interval characterized by a general decrease in the concentrations of various transition metals, including Fe, Mo and Cu. Both Fe(III) and Mn(IV) reduction occur in this zone consisting of the surficial living mat and sediments immediately below, with solid-phase Fe concentrations being about one order of magnitude higher than Mn. The log D trend of Cu closely parallels that of Mo ($r_S = 0.92$, $p < 0.001$) (Fig. 3). The trend in Mo and Cu depletion also correlates with that of TOC ($r_S = 0.54$, $p < 0.001$) and C/N values ($r_S = 0.68$, $p < 0.001$), pointing to the role of organic matter as a sink for these metals. The base of this chemofacies is a local minimum in all solid phase redox sensitive metals (Fig. 3).

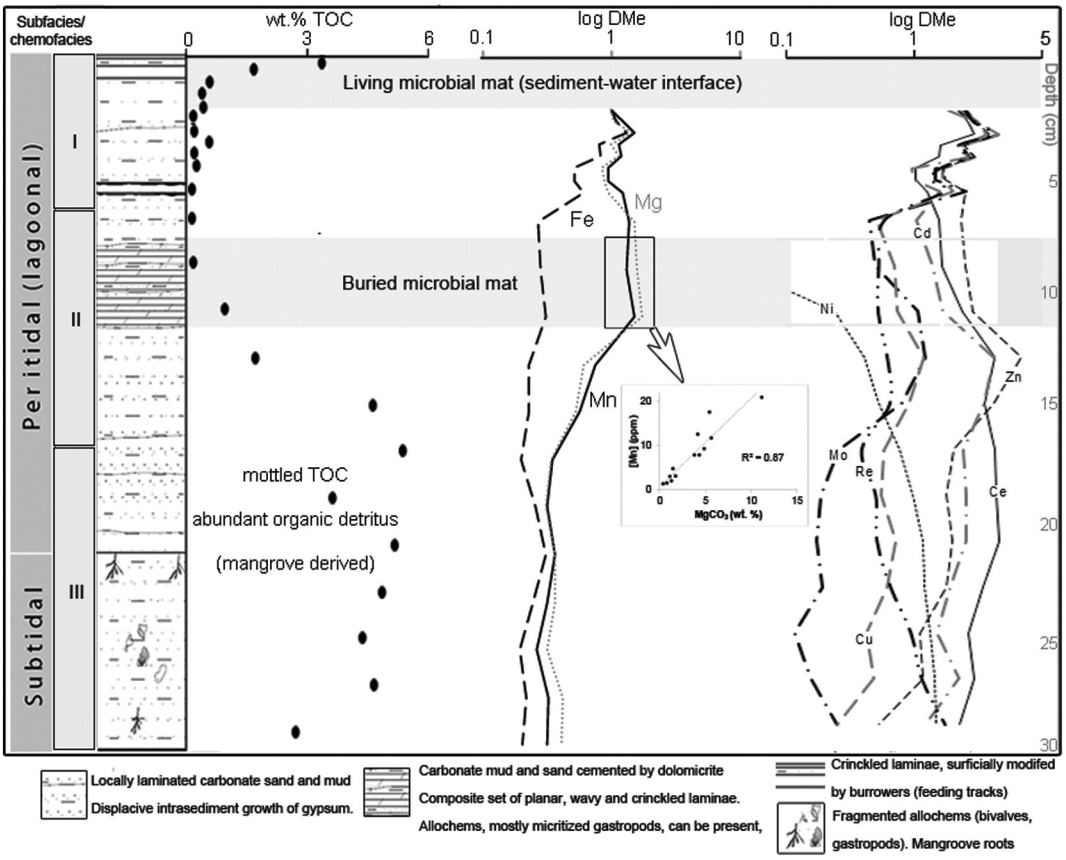

Fig. 3. Bulk sedimentological and geochemical trends along the studied interval. TOC values of the lagoonal facies range from 0.24 to 4.56 wt.%. In the first 10 cm of the sedimentary pile, TOC is approximately equal to the reciprocal of depth$^{-1/2}$; a significant increase in TOC values occurs below 11 cm depth. The bulk sediment trace metal enrichment/depletion trends were normalized using concentrations measured at the microbial mat sediment interface ($D_{Me} = ([Me]_{Sed} / [Me]_{lw}) \cdot ([Ca]_{lw} / [Ca]_{Sed})$, see also Table 1). Areas influenced by the microbial mats are shown in light grey, with darker grey showing the living surficial microbial mat.

4.2.2. Chemofacies II

Below Chemofacies I is a transitional zone, from ~6 to 12 cm depth, which spans the dolomite-bearing buried microbial mat horizon, and in which bulk sediment Mn exhibits a concentration maximum concomitant with decreased bulk sediment Fe concentration and relatively low concentrations of Mo and Cu (Fig. 3). Chemofacies II exhibits peak bulk sediment Mg concentrations (as MgO) up to 18.9 mol%, with remarkable correspondence between both D_{Me} of Mn and Mg (determined from bulk solid and aqueous phase analyses; Fig. 3), as well as the Mn and Mg contents of high-Mg calcite cements (as determined by laser ablation ICP-MS; Fig. 3 inset). The base of this zone marks a subsequent increase in TOC.

4.2.3. Chemofacies III

This zone is defined as being from the base of Chemofacies II to at least 30 cm depth. At the top, bulk sediment concentrations of Zn and Cd are at their highest (Fig. 3). The top is also characterized by mottled organic matter-rich zones and exhibits a local maximum in Mo and Cu concentrations. Chemofacies III shows relatively constant concentrations of Fe, which contrast with the progressive depletion of solid-phase Mn. Nickel and cobalt rise above our instrumental detection limits (Fig. 3) indicating that these elements may be dependent on the rates of Fe(III) and Mn(IV)-reduction. These trends are accompanied by increasing concentrations of Cr, V, and U (not shown), whose geochemical behaviours are strongly correlated (r_S = 0.84 to 0.93,

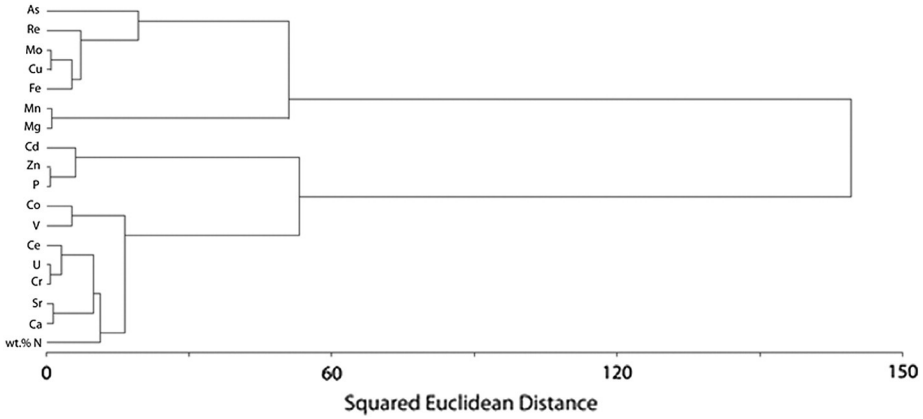

Fig. 4. Dendrogram representing the outcome of a hierarchical cluster analysis of bulk sediment composition (fraction soluble in 8 M HNO_3, thus excluding refractory detrital minerals).

$p < 0.001$) with those of the redox sensitive element Re. This redox sensitive element increases progressively towards the base, peaking at about 22 cm below the water–sediment interface. The down core distribution of solid phase-bound Re allows for the identification of the most reducing intervals.

4.3. Ca-dolomite distribution

A buried microbial mat hosting a laminar dolomite-bearing horizon was observed at a depth between 8 and 12 cm below the sediment water interface (Fig. 3). At this interval, the mineral assemblage consists of halite, partially replaced gypsum, and aragonite. They are cemented by microcrystalline high Mg calcite and disordered Ca-dolomite. The latter occurs interstitially as spheroidal aggregates composed of sub-micrometer-scale rhombs that are in direct contact with decaying EPSs (Fig. 5A). WDS analyses show that the proportion of $CaCO_3$ in micritic Ca-dolomite is between 57.8 and 60.1 wt.% (Fig. 5B).

Changes in TOC (Fig. 3), total nitrogen (not shown), and Mg, Fe, and Mn concentration depth profiles (Figs. 3 and 5C), point to a link between heterotrophy, the bulk-sediment abundance of Ca-dolomite, and these elements. Also, within a chemostratigraphic context, it was observed that Zn, Mo, Re, Cu, and As are enriched immediately below the dolomite-cemented interval (see Fig. 3). The co-enrichment of siderophile and chalcophile metals at this level suggests co-precipitation with solid phase sulfide minerals, such as pyrite. However, neither pyrite nor its precursor monosulfide phases were observed, and if present, they were below the detection limit of standard XRD analyses (~2 wt.%). On this note, a closer observation to the bulk sediment concentration trends (Table 1) shows strong correlation ($r_S = 0.907 \pm 0.030$, $p < 0.001$) between chalcophile elements (e.g., Zn and Cd) with P, but not between these elements and Fe (Fig. 4). This result points to metal scavenging potential by another mineral phase, such as Ca-hydroxyapatite (e.g., Seaman et al., 2001). The latter occurs as small sub-millimeter-scale concretions below the dolomite-cemented interval (Fig. 6).

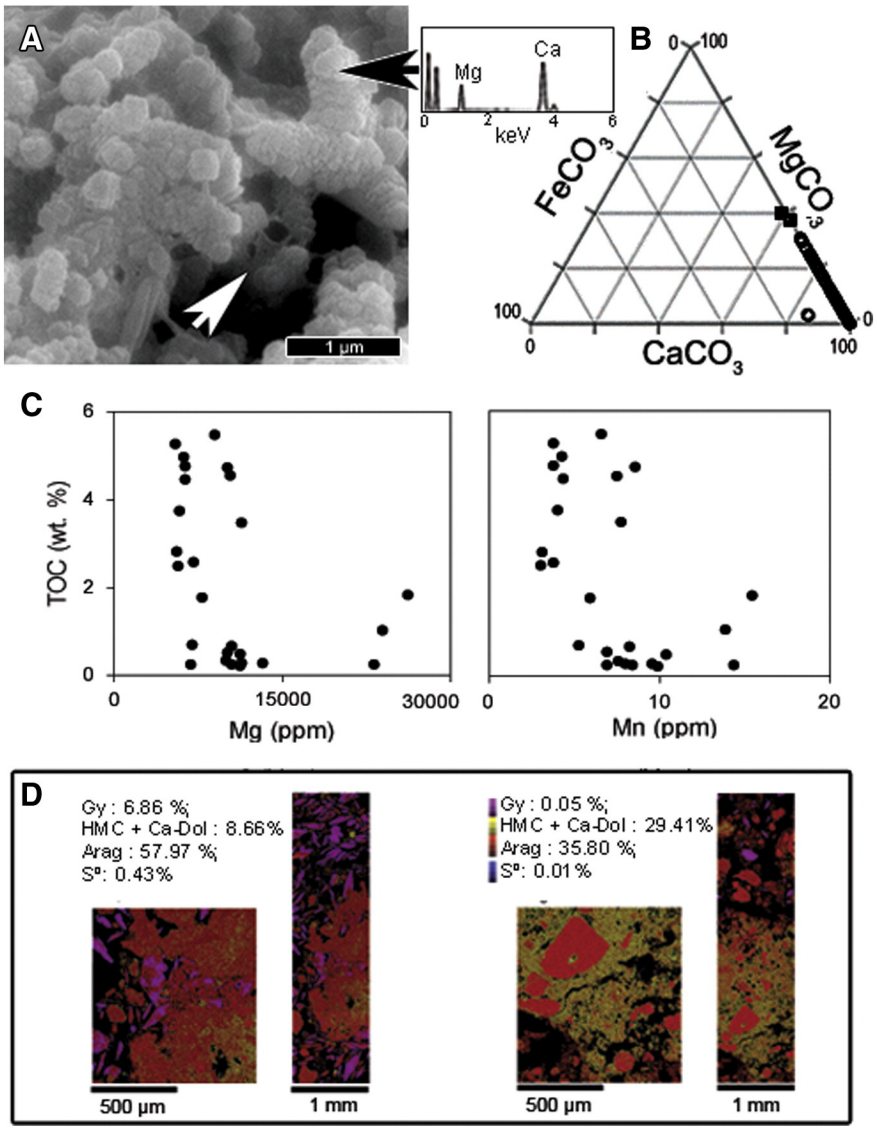

Fig. 5. Textural and electron probe microanalyses of the dolomite-bearing interval. A: High magnification SEM photomicrograph and EDS spectrum of the Ca-dolomite cements, the latter associated with decaying EPS (arrow). B: $MgCO_3$–$CaCO_3$–$FeCO_3$ triangular plot of cement composition based on WDS data. C: More efficient degradation of sedimentary organic matter is observed in the Mg and Mn enriched interval (data from ICP-MS). D: Backscattered electron imaging and composite Ca, S, and Mg elemental maps (EMPA) provide evidence for the replacement of gypsum by aragonite, and the distribution of Ca-dolomite and elemental sulfur in the 8–10 cm depth interval. Note the decrease in S^0 accumulation in interstitial areas occluded by Mg-enriched carbonates.

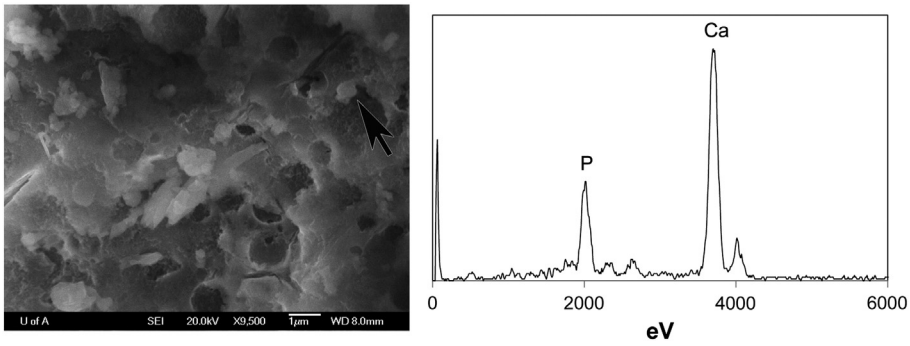

Fig. 6. SEM micrograph and EDS spectrum of Ca-hydroxyapatite at 13-cm depth.

Petrographic relationships revealed by EPMA indicate that S^0 has accumulated in zones texturally dominated by gypsum and aragonite, while interstitial zones are being occluded by a mixture of microcrystalline Mg-enriched carbonate cements that lack S^0 accumulations (Fig. 5D). In order to evaluate the association between Ca-dolomite, Mn accumulations and S^0 depletion, the solid phase chemostratigraphic data were complemented by a number of high resolution in situ analyses, including LA-ICP-QMS, μXRD, μXRF and μXANES. With a spatial resolution (spot size diameter) of 40 μm, our laser ablation data shows a striking correlation between the concentrations of Mn and Mg (see Fig. 3 inset). The integration of our μXRD analyses with μXRF (spatial resolution = 5 × 6 μm) also reveals the co-occurrence of microcrystalline Ca-dolomite (d_{104} = 2.901 Å), high-Mg calcite, and aragonite in association with solid phase accumulations of manganese (Figs. 7 and 8). Unfortunately, defining the exact mineralogy of Mn-bearing phases is precluded by the poor crystallinity of the mineral phases comprising these heterogeneous cements and their nanometer crystal size. Moreover, the presence of calcite makes it difficult to detect small amounts of Mn(II)-bearing carbonate phases (cf. Table 2). It is important to note that although thermodynamically predicted, no Ca-dolomite was positively identified in sediments directly influenced by the decaying process of the surficial photosynthetic microbial mat system. Indeed, in this peritidal parasequence, the mineral was only identified in the suboxic zone influenced by the subsurface decay of a buried microbial mat.

4.4. Evidence for multiple manganese redox states

Electron probe microanalyses demonstrate that the interstitial distribution of Ca-dolomite is accompanied by a decrease in solid-phase sulfur (Fig. 5D). Synchrotron-based microanalyses, on the other hand, reveal that Mn occurs in interstitial areas being occluded by heterogeneous carbonate cements (Figs. 7 and 8), and that other transition metals, known for their affinity for reactive manganese species (e.g., Ni, Co, and Zn), are spatially related with the Mn accumulations (Fig. 8; Table 3). XANES further provides information about the mineralogy of the Mn-bearing phases, as well as the Mn redox states. The presence of Mn(III) is evident by the position and broad white line feature of the K-edge, which exhibits two peaks at 6545.0 and 6548.5 eV (Fig. 9A, B). A linear combination fit of the sorption edge is only achieved by including Mn_2O_3, $MnCO_3$, -MnOOH, and Mn_3O_4 as standards (Fig. 9C). From the semi-quantitative analysis of the resulting Mn–K edge spectrum it can be concluded that in the dolomite-bearing interval, most manganese occurs interstitially as mixed-valence state oxide minerals, yet a substantial fraction of reduced Mn^{2+} may substitute for Mg^{2+} in the micritic carbonates.

4.5. Mn cycling as a factor promoting dolomite stabilization?

Several lines of evidence suggest that dolomite growth in the Francisqui lagoon was more likely promoted by cycling of metals (specifically Mn) as opposed to metabolisms more commonly implicated in dolomite formation, such as sulfate reduction or methanotrophy. These include (1) the strong correspondence between sedimentary Mn and $MgCO_3$ enrichments throughout the sedimentary pile, (2) tight correspondence between Mg and Mn contents in micrite cements in the dolomite-cemented interval, and (3) the co-occurrence of elemental sulfur with Mn in multiple valence states in the dolomitized interval. The dolomite cemented interval occurs at significant depth (8–12 cm) below the sediment–water interface, it is restricted to the buried mat, and is located well within the zone of sulfate reduction. These features all point towards the fact that the nucleation of dolomite may not actually be occurring at present, but rather occurred as the microbial mat hosting the dolomitized interval was buried. The strong correspondence between Mn and $MgCO_3$ in bulk sediments and micritic cements, combined with the presence of Mn in mixed valence states in the dolomite interval, suggests an important role for Mn cycling during early diagenetic dolomite growth. Below we expand on the potential operation

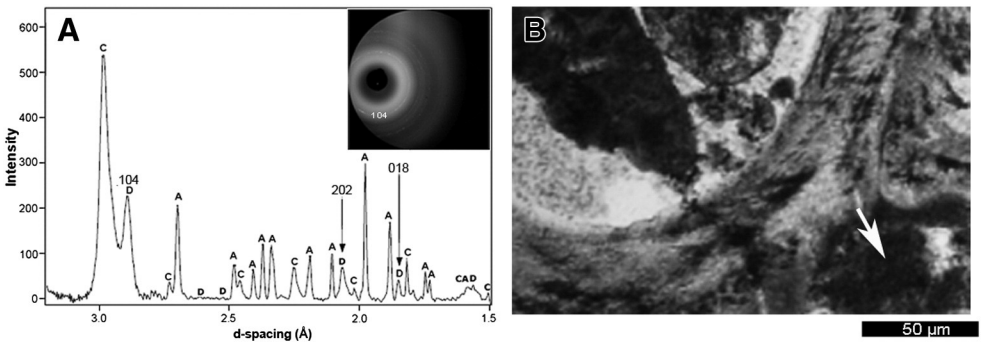

Fig. 7. Synchrotron-based μ-XRD. A: Close up of the 2D integrated pattern (inset) obtained over the analytical area (~30 μm^2) shown in B (arrow) at this location. The dominant phases are microcrystalline high-Mg calcite, aragonite, and Ca-dolomite (d_{104} = 2.901 Å). B: SEM micrograph showing a micritized hydrobiid gastropod shell and associated micritic cements. See also Fig. 8.

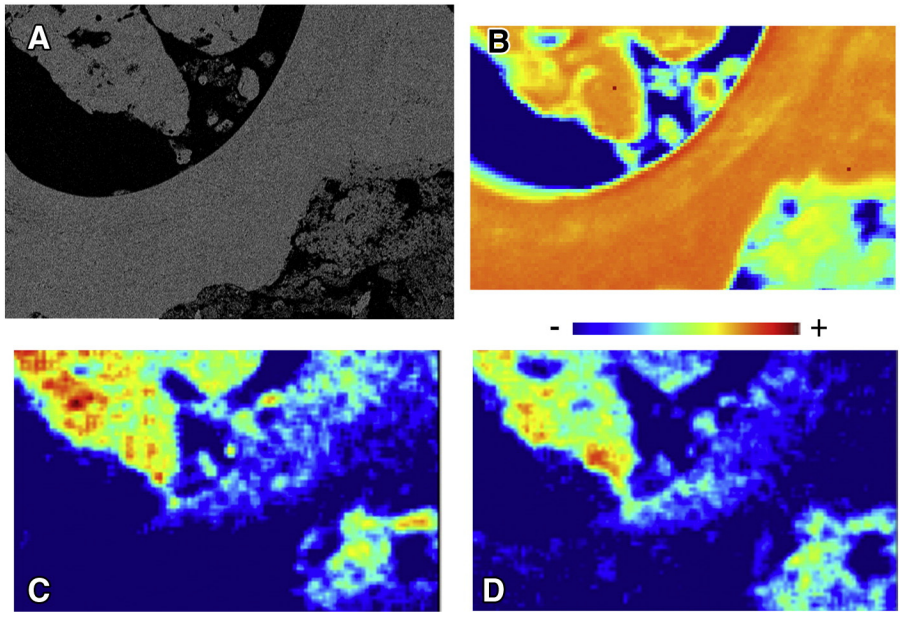

Fig. 8. Micro-XRF distribution maps (400 × 600 μm^2) showing zones of preferential enrichment of Ca (B), Mn (C), and Ni (D) in the cements. The color-coding convention is presented on the scale bar (300 μm in size); it assigns blue to the minimum and red to maximum deconvoluted peak area of the element. (For interpretation of the references to color in this figure legend, the reader is referred to the web version of this article.)

and efficiency of Mn-driven diagenetic reactions that would act to favor dolomitization.

As in surface ocean waters, most dissolved manganese in the lagoon is thought to be maintained in its divalent state (i.e., Sunda and Huntsman, 1988, 1990) due to its slow oxidation rate in the presence of O_2 (Murray and Brewer, 1977). Therefore, Mn^{2+} may potentially form organo-metallic complexes with reactive ligands of the microbial mat (i.e., Petrash et al., 2011a,b). Nonetheless, Mn(II)-oxidizing bacteria could be highly active under conditions of low oxygen, as shown in other hypersaline systems (e.g., Tebo, 1991). Previous work has also shown that both Mn_3O_4 and MnOOH are the primary products of enzyme-catalyzed Mn(II) oxidation reactions (Hastings and Emerson, 1986; Mann et al., 1988; Bargar et al., 2000). These phases may then transform into Mn(IV) oxides abiotically, via the autocatalytic oxidation of Mn(III), leading to disproportionation (Bargar et al., 2000; Tebo et al., 2004). Nucleation of both primary and secondary Mn-bearing oxide phases may also be catalyzed by organic and inorganic ligands comprising microbial mats (i.e., Haack and Warren, 2003). The rapid burial of reactive microbial mats in peritidal settings can thus enable a cascade of aqueous reactions involving intermediate and reduced forms of manganese and sulfur that allow the metal to be recycled multiple times (Fig. 10).

Upon burial, the Mn (oxy)hydroxide phases within the EPS may become solubilized. After oxygen (and nitrate if available) is consumed, the earliest stage of anaerobic respiration in the sedimentary pile involves the progressive reduction of Mn (oxy)hydroxides to soluble Mn(II) (Burdige and Nealson, 1985; Burdige, 1993; Tebo et al., 2004). This dissolved Mn(II) may influence local mineral saturation with respect to Mn-bearing carbonates (e.g., cf. Mucci, 1988), or may diffuse vertically and/or laterally, to be biologically oxidized back to Mn(IV), sometimes accompanied by the formation of solid phase and potentially mixed-valence Mn oxides, including Mn(III)-bearing intermediates (Burdige and Nealson, 1985; Myers and Nealson, 1988; Calvert and Pedersen, 1996; Tebo et al., 2004; Tribovillard et al., 2006; Trouwborst et al., 2006). When the process is linked to reduced and intermediate sulfur species (e.g., HS^-, S^0), the formation of Mn (oxy)hydroxides promotes reactions that evolve pore-waters towards more alkaline conditions. Indeed, Aller and Rude (1988) demonstrated that in normal marine-derived pore-waters, most alkalinity produced during the reduction of Mn(IV) is rapidly consumed by the co-precipitation of Ca, and some of the reduced Mn(II), into Mg-rich calcites.

Here we suggest that Mn(IV) reduction and recycling may also lead to the precipitation of Ca-dolomite. In our model, the precipitation potential of dolomite is enhanced by the co-occurrence of reduced sulfur species (e.g., HS^-, S^0) and Mn (oxy)hydroxides within the buried microbial mat, i.e., the dolomite-cemented interval. This occurs during reduction of Mn(IV/III) coupled to sulfur oxidation (reactions 1–2) or during Mn(III)-driven elemental sulfur disproportionation (reaction 3) (Thamdrup and Finster, 1993; Böttcher and Thamdrup, 2001; Schippers and Jørgensen, 2001). Moreover, Mn(III) species produced during sulfide oxidation (e.g., reaction 1) are more active in sedimentary diagenesis than previously thought because they can also act as an electron donor (reaction 4) (Trouwborst et al., 2006; Madison et al., 2013).

$$2MnO_2 + HS^- + H_2O \rightarrow 2MnOOH + S^0 + OH^- (\Delta G_r = -96\ \text{kJ/mol}), \quad (1)$$

Table 3
Semi quantitative μ-XRF concentration data (units in ppm).

MCA	Ti	V	Mn	Fe	Co	Ni	Cu
Zone A (micritized snail)							
1-1	1.11	1.52	5.82	71.71	0.41	1.16	1.03
1-2	0.80	2.70	3.63	40.87	0.93	1.13	0.52
1-3	0.32	0.25	2.31	41.47	1.34	0.17	0.69
1-4	0.33	0.25	2.66	42.01	1.36	0.17	0.70
1-5	0.44	1.14	1.12	34.59	1.39	0.14	0.37
1-6	1.74	0.96	5.22	35.99	0.36	0.88	0.43
SD	0.56	0.92	1.80	13.71	0.48	0.50	0.24
Zone B: (microcrystalline dolomite-bearing cements)							
2-1	0.78	0.69	19.96	71.51	3.58	0.12	0.75
2-2	0.28	1.63	18.89	118.31	1.85	0.22	0.73
2-3	1.98	0.28	31.93	156.72	5.57	0.15	1.31
2-4	0.17	0.46	21.26	343.04	2.36	4.49	1.36
2-5	1.30	2.74	18.98	130.38	7.94	0.57	0.56
SD	0.75	1.03	5.52	104.74	2.51	1.90	0.37

Units are ppm. Measured in an area of 6 × 5 μm.

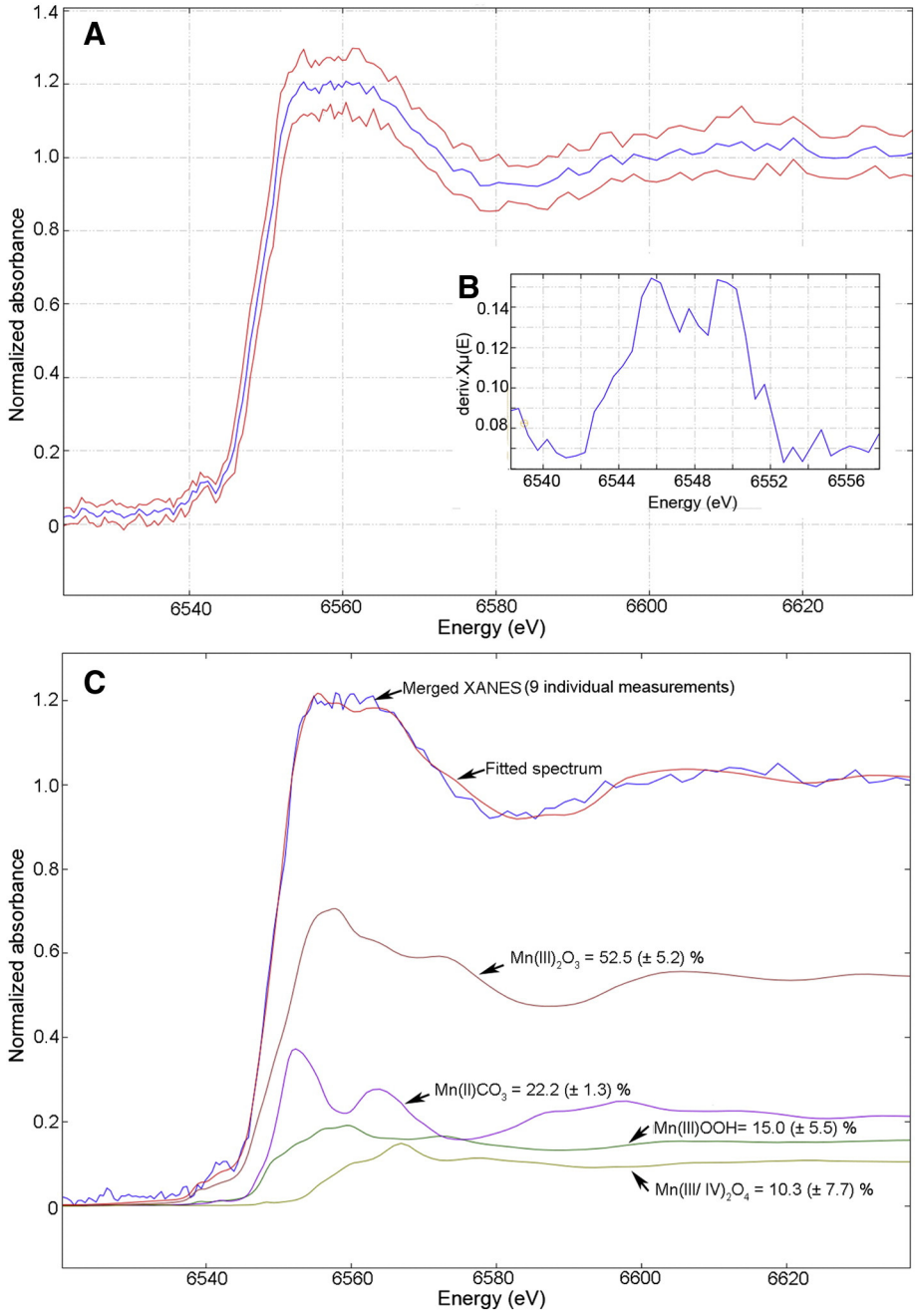

Fig. 9. Normalized Mn K-edge merged spectra of the analytical area shown in Fig. 7B (arrow). A. The K-edge exhibits two main features at about 6554 and 6558 eV. B: Intermediate valence Mn(III) is identified by using the first derivative of the XANES spectra in the interval 6547.9–6549.0 eV (e.g., Manceau et al., 2012). C: A least-square fitting of the spectra was performed to quantify the Mn species present. The spectra can be fitted with four model compounds, Mn_2O_3 (52.5 ± 5.2%), $MnCO_3$ (22.2 ± 1.3%), -MnOOH (15.0 ± 5.0%), and Mn_3O_4 (10.3 ± 7.7%), suggesting that co-occurrence of these phases in the dolomite-bearing microcrystalline cements.

$$3MnO_2 + S^0 + 2H_2O \rightarrow SO_4^{2-} + 3Mn^{2+} + 4OH^- (\Delta G_r = -107 \text{ kJ/mol}), \quad (2)$$

$$Mn_3O_4 + 3S^0 + 2H^+ \rightarrow 3Mn^{2+} + SO_4^{2-} + 2HS^- (\Delta G_r = -118 \text{ kJ/mol}), \quad (3)$$

$$2MnOOH + 2H^+ \rightarrow MnO_2 + Mn^{2+} + 2H_2O (\Delta G_r = -51 \text{ kJ/mol}). \quad (4)$$

These redox reactions are relevant in suboxic near-shore sediments where intermediate and reduced sulfur species are brought into close contact with Mn (oxy)hydroxides by natural depositional or syndiagenetic processes (Aller, 1990). They collectively act to increase total alkalinity (see Aller and Rude, 1988), and as experimentally demonstrated by Böttcher and Thamdrup (2001), also lead to a continuous increase in pH (e.g., reactions 1–4). However, for dolomite saturation, equally or perhaps even more important is their role in recycling Mn and assuring for a steady upwards diffusive supply and continual oxidation of Mn^{2+}. This, in turn, yields Mn(IV) oxides that can be reduced anew to sustain long-term conditions that — because of the high Mg/Ca ratios of the precipitation microenvironment — may be favorable for dolomite growth. Importantly, our semi-quantitative

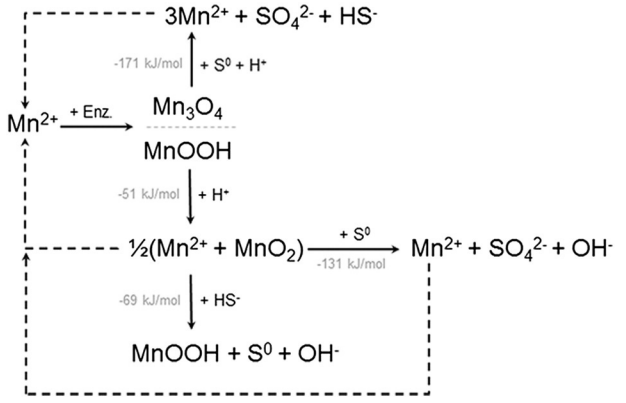

Fig. 10. Schematic showing a simplified coupled sedimentary manganese–sulfur cycle as envisioned in the dolomite-cemented interval associated with the buried microbial mat. Theoretical calculation of energy yield of each reaction is also shown. (This diagram is not mass or charge balanced. See details in text: reactions 1–4.)

XANES analyses showed that although some of the Mn^{2+} diffuses upwards where it could be re-oxidized, a fraction of it substitutes for Mg into newly formed Ca-dolomite (cf. Fig. 9), leaving the imprint of Mn cycling that we believe we are observing in the dolomite cemented interval at Francisqui lagoon. Using published Mn partitioning coefficients (K_D) for carbonates in the rhodochrosite–calcite solid solution series (Mucci, 1988; Böttcher, 1998), we estimate maximal pore-water Mn concentrations during carbonate mineral precipitation at between 50 and 700 μM (depending on the K_D), which fall within the range observed in Mn carbonate-rich sediments where Mn cycling dominates the pore-water alkalinity budget (e.g., Thamdrup and Dalsgaard, 2000).

When coupled to the utilization of sedimentary organic matter (e.g., from the buried microbial mat), Mn(IV) reduction (reaction 5) is more efficient than acetoclastic bacterial sulfate reduction (BSR) at generating alkalinity (reaction 6). In the presence of intermediate forms of sulfur, the process may continuously consume protons to sustain elevated pH levels in the precipitation environment. Such precipitation conditions have long been thought required for interstitial dolomite nucleation (Lippmann, 1973; Middelburg et al., 1990; Mazzullo, 2000).

$$CH_3COO^- + 4MnO_2 + 3H_2O \rightarrow 4Mn^{2+} + 2HCO_3^- + 7OH^- \quad (\Delta G_r = -569\ \text{kJ/mol}), \tag{5}$$

$$CH_3COO^- + SO_4^{2-} + H_2O \rightarrow H_2S + 2HCO_3^- + OH^- \quad (\Delta G_r = -48\ \text{kJ/mol}). \tag{6}$$

A key point in this regard is whether or not the relatively low Mn concentrations characterizing most marine sediments are capable of generating sufficient alkalinity as to locally influence carbonate mineral saturation. Previous data for atypical marine sediments where Mn(IV), rather than sulfate, serves as the primary terminal electron acceptor for anaerobic respiration indicates that very little Mn is required. For example, Canfield et al. (1993a,b) demonstrated that in Danish sediments with solid-phase Mn concentrations roughly two orders of magnitude higher than reported herein, Mn(IV) was more important for respiration, and by proxy the alkalinity budget, than all other electron acceptors combined, including oxygen, by a factor of ~10. In this environment, Mn(IV) reduction accounts for 25–99% of anaerobic carbon oxidation in the upper 10 cm of sediments. Part of the reason is rampant Mn recycling; Mn(IV) is continually regenerated by either spontaneous disproportionation of Mn(III) or by aerobic oxidation of Mn(II), the latter being the product of Mn(IV) reduction and also Mn(III) disproportionation (see reactions 1–4; Fig. 10). In this manner, seemingly small sedimentary Mn enrichments may have contributed to the general underestimation of the role of Mn in organic matter cycling (cf. Canfield et al., 1993a; Sunda and Kieber, 1994), and thus alkalinity generation.

Based on our observations at this novel dolomite-forming site, we speculate that in peritidal settings the burial of metal-reactive microbial mats may act as a barrier capable of localizing upward diffusing species in an autocatalytic feedback between Mn (oxy)hydroxide precipitation, solid phase sulfide dissolution, and carbon turnover (Fig. 10). While we consider adsorption of Mn to the reactive mat substrate (promoting greater Mn residence times in the suboxic manganic zone) a microbially-influenced process (cf. Dupraz et al., 2009), we consider Ca-dolomite formation in this setting effectively a microbially-induced process (cf. Dupraz et al., 2009), whereby the initial standing stock of reactive manganese and its efficient redox cycling sustain the elevated alkalinities promoting Ca-dolomite growth. Importantly, as this biochemical process takes place, the rapid oxidation of diffused HS^- (reaction 1) may also act to alleviate the inhibitory effect of Mg coordination by water at the solution–solid interface (see Zhang et al., 2012, and also Yang et al., 2012), and ultimately facilitate interstitial Ca-dolomite growth. It is important to also note that abundant Mn cycling is not likely sufficient on its own; higher initial dissolved Mg/Ca, such as occurs in Francisqui lagoon (~6.1), is likely important in that it kinetically favors the formation of Ca-dolomite.

The influence of the water activity (a_w) on the crystallization of Mg-rich carbonates may also be important for the precipitation of dolomite precursors. In experiments where this effect has been tested (i.e., at a_w below the life limit, <0.72), the resulting solid phases are a mixture of magnesian calcite, aragonite, and hydromagnesite, but no dolomite (e.g., Lenders et al., 2012; Radha et al., 2012). The hydrated Mg oxides in such experiments attest to the strong binding of the first hydration shell to Mg. In hypersaline systems where the activity of water does not prevent the growth of microbial life, hydrated Mg oxides are only found in supratidal zones at very high evaporation rates. In such environments, the removal of Ca^{2+} due to the precipitation of gypsum ($CaSO_4 \cdot 2H_2O$) contributes to a rise in pore water Mg/Ca ratios. It also consumes sulfate from the water column, making it available as an electron acceptor in subsequent shallow burial diagenetic reactions (i.e., Petrash et al., 2012). Gypsum reduction also facilitates dolomitization because it creates high alkalinity via the oxidation of the sedimentary organic matter, and the carboxylic acids liberated can serve as nucleation templates (Kenward et al., 2013; Roberts et al., 2013).

The high dissolved Mg/Ca ratios in our study site clearly favor the precipitation of Mg-rich carbonate, but not Mn-rich carbonate-bearing phases, which are more common in sediments exposed to relatively low open marine Mg/Ca ratios and much higher Mn concentrations. Because the mechanism for sustained alkalinity described here would coincide with a zone of relatively high dissolved sulfide concentrations, it is possible that some of the early microbial models ascribing a prominent role to BSR might in fact be much more complicated and involve Mn (and S) cycling. As recently suggested by Meister (2013), BSR alone might be ineffective for inducing carbonate saturation (but see Gallagher et al., 2012), and only with an alternative mechanism acting in parallel would BSR lead to a state of localized dolomite supersaturation (i.e., Moreira et al., 2004).

5. Summary and conclusions

At Francisqui, a buried microbial mat appears to have facilitated authigenic dolomite precipitation in three ways: (1) by providing a highly reactive substrate for initial Mn and Mg sorption, (2) by providing the reducing equivalents (as organic carbon) for driving heterotrophic reactions that promote alkalinity and carbonation of Mg ions, and (3) upon rapid burial, bringing the Mn-rich, diffusion-limited mat substrate into the sulfate reduction zone where coupled Mn–S redox cycling auto-catalytically enhanced alkalinity generation given sufficient organic matter. We suggest here that these processes have the

potential to locally increase pH and alkaline conditions, which together with relatively high Mg:Ca ratios observed in the lagoon water and inferred for the pore-waters, fulfills the prerequisites for the interstitial stabilization (and growth) of early formed dolomite precursors in shallow burial diagenetic realms. More detailed studies on classic penecontemporaneous dolomite-forming settings should consider the importance of manganese cycling in dolomite authigenesis and the integral role of subsurface microbes in shallow burial dolomite formation.

Supplementary data to this article can be found online at http://dx.doi.org/10.1016/j.chemgeo.2015.03.017.

Acknowledgments

The authors wish to thank three anonymous reviewers who provided constructive criticisms and comments that greatly improved this manuscript, and to Dr. Michael E. Böttcher for his scientific input and guidance through the editorial process. Funds for this research were provided by the National Science and Engineering Research Council of Canada (NSERC) granted to K.O.K. S.V.L. acknowledges support from NSERC and LabexMER. Sector 20 facilities at the Advanced Photon Source, and research at these facilities, are supported by the US Department of Energy — Basic Energy Sciences, the Canadian Light Source and its funding partners, the University of Washington, and the Advanced Photon Source. Use of the Advanced Photon Source, an Office of Science User Facility operated for the U.S. Department of Energy (DOE) Office of Science by Argonne National Laboratory, was supported by the U.S. DOE under Contract No. DE-AC02-06CH11357. We also thank Dr. Lachlan McLean, Dr. Ferenc Borondics (and the team members of the mid-IR (01B1-1) beamline) at the Canadian Light Source for technical advice and support, as well as Dr. François Orange for his support with TEM.

References

Aller, R.C., 1990. Bioturbation and manganese cycling in hemipelagic sediments. Phil. Trans. R. Soc. A 331, 51–68.
Aller, R.C., 1994. The sedimentary Mn cycle in Long Island Sound. Its role as intermediate oxidant and the influence of bioturbation, O_2, and C_{org} flux on diagenetic reaction balances. J. Mar. Res. 52, 259–295.
Aller, R.C., Rude, P.D., 1988. Complete oxidation of solid phase sulfides by manganese and bacteria in anoxic marine sediments. Geochim. Cosmochim. Acta 52, 751–765.
Arvidson, R.S., MacKenzie, F.T., 1999. The dolomite problem: control of precipitation kinetics by temperature and saturation state. Am. J. Sci. 299, 257–288.
Ball, J.W., Nordstrom, K., 1991. User's manual for WATEQ4F, with revised thermodynamic data base and test cases for calculating speciation of major, trace, and redox elements in natural waters. U.S. Geological Survey Open-file Report 91-183.
Bargar, J., Tebo, B., Villinski, J., 2000. In situ characterization of Mn (II) oxidation by spores of the marine *Bacillus* sp. strain SG-1. Geochim. Cosmochim. Acta 64, 2775–2778.
Böttcher, M.E., 1998. Manganese (II) partitioning during experimental precipitation of rhodochrosite–calcite solid solutions from aqueous solutions. Mar. Chem. 62 (3), 287–297.
Böttcher, M., Thamdrup, B., 2001. Anaerobic sulfide oxidation and stable isotope fractionation associated with bacterial sulfur disproportionation in the presence of MnO_2. Geochim. Cosmochim. Acta 65, 1573–1581.
Boyanov, M.I., Kelly, S.D., Kemner, K.M., Bunker, B.A., Fein, J.B., Fowle, D.A., 2003. Adsorption of cadmium to *Bacillus subtilis* bacterial cell walls: a pH-dependent X-ray absorption fine structure spectroscopy study. Geochim. Cosmochim. Acta 67, 3299–3311.
Braissant, O., Decho, A.W., Dupraz, C., Glunk, C., Przekop, K.M., Visscher, P.T., 2007. Exopolymeric substances of sulfate-reducing bacteria: interactions with calcium at alkaline pH and implication for formation of carbonate minerals. Geobiology 5, 401–411.
Braissant, O., Decho, A.W., Przekop, K.M., Gallagher, K.L., Glunk, C., Dupraz, C., Visscher, P.T., 2009. Characteristics and turnover of exopolymeric substances in a hypersaline microbial mat. FEMS Microbiol. Ecol. 67, 2005–2008.
Breuker, A., Stadler, S., Schippers, A., 2013. Microbial community analysis of deeply buried marine sediments of the New Jersey shallow shelf, IODP Expedition 313. FEMS Microbiol. Ecol. http://dx.doi.org/10.1111/1574-6941.12146.
Burdige, D.J., 1993. The biogeochemistry of manganese and iron reduction in marine sediments. Earth Sci. Rev. 35, 249–284.
Burdige, D.J., Nealson, K.H., 1985. Microbial manganese reduction by enrichment cultures from coastal marine sediments. Appl. Environ. Microbiol. 50, 491–497.
Calvert, S.E., Pedersen, T.F., 1996. Sedimentary geochemistry of manganese: implications for the environment of formation of manganiferous black shales. Econ. Geol. 91, 36–47.
Canfield, D.E., Thamdrup, B., Hansen, J.W., 1993a. The anaerobic degradation of organic matter in Danish coastal sediments: iron reduction, manganese reduction, and sulfate reduction. Geochim. Cosmochim. Acta 57, 3867–3883.
Canfield, D.E., Jørgensen, B.B., Fossing, H., Glud, R., Gundersen, J., Ramsing, N.B., Thamdrup, B., Hansen, J.W., Nielsen, L.P., Hall, P.O.J., 1993b. Pathways of organic carbon oxidation in three continental margin sediments. Mar. Geol. 113, 27–40.
Castanier, S., Métayer-Levrel, G. Le, Perthuisot, J., 1999. Ca-carbonate precipitation and limestone genesis — the microbiogeologist point of view. Sed. Geol. 126, 9–23.
Compton, J., 1992. Early diagenesis and the origin of diagenetic carbonate in sediment recovered from the Argo Basin, Northeastern Indian Ocean, Site 765. Proceedings of the Ocean Drilling Program, Site 765, pp. 77–88.
Covington, A.K., Whitfield, M., 1988. Recommendations for the determination of pH in sea water and estuarine waters. Pure Appl. Chem. 60, 865–870.
Curtis, C.D., Cope, J.C.W., Plant, D., Macquaker, J.H.S., 2000. "Instantaneous" sedimentation, early microbial sediment strengthening and a lengthy record of chemical diagenesis preserved in Lower Jurassic ammonitiferous concretions from Dorset. J. Geol. Soc. 157, 165–172.
Davies, P., Ferguson, J., Bubela, B., 1975. Dolomite and organic material. Nature 255, 472–474.
Decho, A.W., 2000. Microbial biofilms in intertidal systems: an overview. Cont. Shelf Res. 20, 1257–1273.
Decho, A.W., Visscher, P.T., Reid, R.P., 2005. Production and cycling of natural microbial exopolymers, EPS, within a marine stromatolite. Palaeogeogr. Palaeoclimatol. Palaeoecol. 219, 71–86.
Défarge, C., Trichet, J., Jaunet, A.M., Robert, M., Sansone, F.J., 1996. Texture of microbial sediments revealed by cryo-scanning electron microscopy. J. Sed. Res. 66, 935–947.
Des Marais, D.J., 2003. Biogeochemistry of hypersaline microbial mats illustrates the dynamics of modern microbial ecosystems and the early evolution of the biosphere. Biol. Bull. 204, 160–167.
Drever, J.I., 1988. The Geochemistry of Natural Waters. 2nd ed. Prentice-Hall, Englewood Cliffs, New Jersey (437 pp.).
Dupraz, C., Reid, R.P., Braissant, O., Decho, A.W., Norman, R.S., Visscher, P.T., 2009. Processes of carbonate precipitation in modern microbial mats. Earth-Sci. Rev. 96, 141–162.
Fein, J., Daughney, C., Yee, N., Davis, T., 1997. A chemical equilibrium model for metal adsorption onto bacterial surfaces. Geochim. Cosmochim. Acta 61, 3319–3328.
Filzmoser, P., Hron, K., 2008. Outlier detection for compositional data using robust methods. Math. Geosci. 40, 233–248.
Fraústo da Silva, J.J.R., Williams, R.J.P., 2001. The Biological Chemistry of the Elements. second ed. Oxford University Press, Oxford, UK (575 pp.).
Froelich, P.N., Klinkhammer, G.P., Bender, M.L., Luedtke, N.A., Heath, G.R., Cullen, D., Dauphin, P., Hammond, D., Hartman, B., Maynard, V., 1979. Early oxidation of organic–matter in pelagic sediments of the eastern equatorial Atlantic: suboxic diagenesis. Geochim. Cosmochim. Acta 43, 1075–1090.
Gallagher, K.L., Kading, T.J., Braissant, O., Dupraz, C., Visscher, P.T., 2012. Inside the alkalinity engine: the role of electron donors in the organomineralization potential of sulfate-reducing bacteria. Geobiology 10, 518–530.
Gebelein, C.D., Hoffman, P., 1973. Algal origin of dolomite laminations in stromatolitic limestone. J. Sediment. Petrol. 43, 603–613.
Geesey, G.G., Jang, L., 1989. Interactions between metal ions and capsular polymers. In: Beveridge, T.J., Doyle, R. (Eds.), Metal Ions and Bacteria, pp. 325–357.
Gilbert, P., Abrecht, M., Frazer, B.H., 2005. The organic–mineral interface in biominerals. Rev. Mineral. Geochem. 59, 157–185.
Glew, J.R., 1991. Miniature gravity corer for recovering short sediment cores. J. Paleolimnol. 5, 285–287.
Haack, E.A., Warren, L.A., 2003. Biofilm hydrous manganese oxyhydroxides and metal dynamics in acid rock drainage. Environ. Sci. Technol. 37, 4138–4147.
Hammersley, A.P., Svensson, S.O., Han, M., Fitch, A.N., Hausermann, D., 1996. Two-dimensional detector software: from real detector to idealized image or two-theta scan. High Press. Res. 14, 235–248.
Hardie, L.A., Shinn, E.A., 1986. Carbonate depositional environments — modern and ancient — part 3. Tidal flats. Colo. Sch. Mines Q. 81, 1–74.
Hastings, D., Emerson, S., 1986. Oxidation of manganese by spores of a marine Bacillus: kinetic and thermodynamic considerations. Geochim. Cosmochim. Acta 50 (8), 1819–1824.
Jones, B., Luth, R., MacNeil, A., 2001. Powder X-ray diffraction analysis of homogeneous and heterogeneous sedimentary dolostones. J. Sediment. Res. 71, 790–799.
Kendall, C.G.St.C., Skipwith, P.S., 1968. Recent algal mats of a Persian Gulf lagoon. J. Sediment. Petrol. 38, 1040–1058.
Kenward, P., Fowle, D.A., Goldstein, R.H., Ueshima, M., González, L.A., Roberts, J.A., 2013. Ordered low-temperature dolomite mediated by carboxyl-group density of microbial cell walls. AAPG Bull. 97, 2113–2125.
Konhauser, K.O., 2007. Introduction to Geomicrobiology. Blackwell Publishing (433 pp).
Kraft, S., Stümpel, J., Becker, P., Kuetgens, U., 1996. High resolution x-ray absorption spectroscopy with absolute energy calibration for the determination of absorption edge energies. Rev. Sci. Instrum. 67, 681–687.
Kwak, S.Y., DiMasi, E., Han, Y.-J., Aizenberg, J., Kuzmenko, I., 2005. Orientation and Mg incorporation of calcite grown on functionalized self-assembled monolayers. A synchrotron X-ray study. Cryst. Growth Des. 5, 2139–2145.
Lalonde, S.V., Konhauser, K.O., Reysenbach, A.-L., Ferris, F.G., 2005. Thermophilic silicification: the role of aquificales in hot spring sinter formation. Geobiology 3, 41–52.
Lalonde, S.V., Amskold, L., McDermott, T.R., Inskeep, W.P., Konhauser, K.O., 2007. Chemical reactivity of microbe and mineral surfaces in hydrous ferric oxide depositing hydrothermal springs. Geobiology 5, 219–234.
Lalonde, S.V., Dafoe, L.T., Pemberton, S.G., Gingras, M.K., Konhauser, K.O., 2010. Investigating the geochemical impact of burrowing animals: proton and cadmium adsorption onto the mucus lining of Terebellid polychaete worms. Chem. Geol. 271, 44–51.

Lenders, J.J.M., Dey, A., Bomans, P.H.H., Spielmann, J., Hendrix, M.M.R.M., de With, G., Meldrum, F.C., Harder, S., Sommerdijk, N.A.J.M., With, G. De, 2012. High-magnesian calcite mesocrystals: a coordination chemistry approach. J. Am. Chem. Soc. 134, 1367–1373.
Lippmann, F., 1973. Sedimentary Carbonate Minerals. Springer-Verlag, Berlin, p. 228.
Madison, A.S., Tebo, B.M., Mucci, A., Sundby, B., Luther, G.W., 2013. Abundant pore-water Mn (III) is a major component of the sedimentary redox system. Science 341, 875–878.
Manceau, A., Marcus, M., Grangeon, S., 2012. Determination of Mn valence states in mixed-valent manganates by XANES spectroscopy. Am. Mineral. 97, 816–827.
Mann, S., Sparks, N.H.C., Scott, G.H.E., deVrind-deJong, E.W., 1988. Oxidation of manganese and formation of Mn_3O_4 (hausmannite) by spore coats of a marine *Bacillus* sp. Appl. Environ. Microbiol. 54, 2140–2143.
Mazzullo, S.J., 2000. Organogenic dolomitization in peritidal to deep-sea sediments. J. Sed. Res. 70, 10–23.
Meister, P., 2013. Two opposing effects of sulfate reduction on carbonate precipitation in normal marine, hypersaline, and alkaline environments. Geology 41, 499–502.
Middelburg, J., de Lange, G.J., Kreulen, R., 1990. Dolomite formation in anoxic sediments of Kau Bay, Indonesia. Geology 18, 399–492.
Montero-Serrano, J.C., Palarea-Albaladejo, J., Martín-Fernández, J.A., Martínez-Santana, M., Gutiérrez-Martín, J.V., 2010. Sedimentary chemofacies characterization by means of multivariate analysis. Sediment. Geol. 228, 218–228.
Moreira, N.F., Walter, L.M., Vasconcelos, C., McKenzie, J.A., Mccall, P.J., 2004. Role of sulfide oxidation in dolomitization: sediment and pore-water geochemistry of a modern hypersaline lagoon system. Geology 32, 701–704.
Mucci, A., 1988. Manganese uptake during calcite precipitation from seawater: conditions leading to the formation of a pseudokutnahorite. Geochim. Cosmochim. Acta 52, 1859–1868.
Murray, J.W., Brewer, P.G., 1977. Mechanism of removal of manganese, iron and other trace metals from seawater. In: Glasby, G.P. (Ed.), Marine Manganese Deposits. Elsevier, Amsterdam, pp. 291–325.
Myers, C.R., Nealson, K.H., 1988. Microbial reduction of manganese oxides. Interactions with iron and sulfur. Geochim. Cosmochim. Acta 52, 2727–2732.
Nordstrom, D.K., Plummer, L.N., Langmuir, D., Busenberd, E., May, H.M., Jones, B.F., Parkhurst, D.L., 1990. Revised chemical equilibrium data for major water–mineral reactions and their limitations. In: Melchior, D.C., Bassett, R.L. (Eds.), Chemical modeling of aqueous systems II. American Chemical Society Symposium Series 416, pp. 398–413.
Parkhurst, D.L., Appelo, C.A.J., 1999. User's Guide to PHREEQC (Version 2) – A Computer Program for Speciation, Batch-Reaction, One-Dimensional Transport, and Inverse Geo- chemical Calculations. US Geological Survey, Denver, CO.
Petrash, D.A., Gingras, M., Lalonde, S.V., Orange, F., Pecoits, E., Konhauser, K.O., 2012. Dynamic controls on accretion and lithification of modern gypsum-dominated thrombolites, Los Roques, Venezuela. Sediment. Geol. 245–246, 29–47.
Petrash, D.A., Lalonde, S.V., Raudsepp, M., Konhauser, K.O., 2011a. Assessing the importance of organic matrix materials in biofilm chemical reactivity: insights from proton and cadmium adsorption onto the commercially available biopolymer alginate. Geomicrobiol J. 28, 266–273.
Petrash, D.A., Lalonde, S.V., Gingras, M.K., Konhauser, K.O., 2011b. A surrogate approach to studying the chemical reactivity of burrow mucous linings in marine sediments. Palaios 26, 594–600.
Ravel, B., Newville, M., 2005. Athena, Artemis, Hephaestus: data analysis for X-ray absorption spectroscopy using IFEFFIT. J. Synchrotron Radiat. 12, 537–541.
Raz, S., Weiner, S., Addadi, L., 2000. Formation of high-magnesian calcites via an amorphous precursor phase: possible biological implications. Adv. Mater. 12, 38–42.
Radha, A.V., Fernandez-martinez, A., Hu, Y., Jun, Y., Waychunas, G.A., Navrotsky, A., 2012. Energetic and Structural Studies of Amorphous Ca1?xMgxCO3?nH2O(0 6 x 6 1) A.V. 90. pp. 83–95.
Roberts, J.A., Kenward, P.A., Fowle, D.A., Goldstein, R.H., González, L.A., Moore, D.S., 2013. Surface chemistry allows for abiotic precipitation of dolomite at low temperature. PNAS 6–11 http://dx.doi.org/10.1073/pnas.1305403110.
Sánchez-Román, M., Mckenzie, J.A., de Luca Rebello, A., Rivadeneyra, M.A., Vasconcelos, C., 2009. Presence of sulfate does not inhibit low-temperature dolomite precipitation. Earth Planet. Sci. Lett. 285, 131–139.
Schippers, A., Jørgensen, B., 2001. Oxidation of pyrite and iron sulfide by manganese dioxide in marine sediments. Geochim. Cosmochim. Acta 65, 915–922.
Seaman, J.C., Arey, J.S., Bertsch, P.M., 2001. Immobilization of nickel and other metals in contaminated sediments by hydroxyapatite addition. J. Environ. Qual. 30, 460–469.
Slaughter, M., Hill, R.J., 1991. The influence of organic matter in organogenic dolomitization. J. Sediment. Petrol. 61, 296–303.
Solé, V.A., Papillon, E., Cotte, M., Walter, Ph., Susini, J., 2007. A multiplatform code for the analysis of energy-dispersive X-ray fluorescence spectra. Spectrochim. Acta B 62, 63–68.
Sunda, W.G., Huntsman, S.A., 1988. Effect of sunlight on redox cycles of manganese in the southwestern Sargasso Sea. Deep-Sea Res. 35, 1297–1317.
Sunda, W.G., Huntsman, S.A., 1990. Diel cycles in microbial manganese oxidation and manganese redox speciation in coastal waters of the Bahama Islands. Limnol. Oceanogr. 35, 325–328.
Sunda, W.G., Kieber, D.J., 1994. Oxidation of humic substances by manganese oxides yields low-molecular-weight organic substrates. Nature 367, 62–64.
Tebo, B.M., 1991. Manganese(II) oxidation in the suboxic zone of the Black Sea. Deep-Sea Res. 38 (Suppl. 2), S883–S905.
Tebo, B.M., Bargar, J.R., Clement, B.G., Dick, G.J., Murray, K.J., Parker, D., Verity, R., Webb, S.M., 2004. Biogenic manganese oxides: properties and mechanisms of formation. Ann. Rev. Earth Planet. Sci. 32, 287–328.
Thamdrup, B., Finster, K., 1993. Bacterial disproportionation of elemental sulfur coupled to chemical reduction of iron or manganese. Appl. Environ. Microbiol. 59, 101–108.
Thamdrup, B., Dalsgaard, T., 2000. The fate of ammonium in anoxic manganese oxide-rich marine sediment. Geochim. Cosmochim. Acta 64, 4157–4164.
Thamdrup, B., Fossing, H., Jørgensen, B., 1994. Manganese, iron and sulfur cycling in a coastal marine sediment, Aarhus Bay, Denmark. Geochim. Cosmochim. Acta 58, 5115–5129.
Tribovillard, N., Algeo, T.J., Lyons, T., Riboulleau, A., 2006. Trace metals as paleoredox and paleoproductivity proxies: an update. Chem. Geol. 232, 12–32.
Trouwborst, R.E., Clement, B.G., Tebo, B.M., Glazer, B.T., Luther, G.W., 2006. Soluble Mn, III, in suboxic zones. Science 313, 1955–1957.
Van Lith, Y., Warthmann, R., Vasconcelos, C., McKenzie, J.A., 2003. Sulphate-reducing bacteria induce low-temperature Ca-dolomite and high Mg-calcite formation. Geobiology 1, 71–79.
Vasconcelos, C., McKenzie, J.A., Bernasconi, S., Grujic, D., Tien, A.J., 1995. Microbial mediation as a possible mechanism for natural dolomite formation at low temperatures. Nature 377, 220–222.
Vasconcelos, C., McKenzie, J.A., 1997. Microbial mediation of modern dolomite precipitation and diagenesis under anoxic conditions (Lagoa Vermelha, Rio De Janeiro, Brazil). J. Sed. Res. 67, 378–390.
Visscher, P.T., Stolz, J.F., 2005. Microbial mats as bioreactors: populations, processes, and products. Palaeogeogr. Palaeoclimatol. Palaeoecol. 219, 87–100.
Von der Borch, C.C., Lock, D., 1979. Geological significance of Coorong dolomites. Sedimentology 26, 813–824.
Wang, D., Wallace, A.F., De Yoreo, J.J., Dove, P.M., 2009. Carboxylated molecules regulate magnesium content of amorphous calcium carbonates during calcification. PNAS 106, 21511–21516.
Warthmann, R., Van Lith, Y., Vasconcelos, C., McKenzie, J.A., Karpoff, A., 2000. Bacterially induced dolomite precipitation in anoxic culture experiments. Geology 28, 1091–1094.
Windom, H.L., Schropp, S.J., Calder, F.D., Ryan, J.D., Smith Jr., R.G., Burney, F.G., Lewis, L.C., Rawlinson, C.H., 1989. Natural trace metal concentrations in estuarine and coastal marine sediments of the southeastern United States. Environ. Sci. Technol. 23, 314–320.
Wright, D.T., 1999. The role of sulphate-reducing bacteria and cyanobacteria in dolomite formation in distal ephemeral lakes of the Coorong region, South Australia. Sediment. Geol. 126, 147–157.
Wright, D.T., Wacey, D., 2005. Precipitation of dolomite using sulphate-reducing bacteria from the Coorong Region, South Australia: significance and implications. Sedimentology 52, 987–1008.
Wright, J.E., Wyld, S.J., 2011. Late Cretaceous subduction initiation on the eastern margin of the Caribbean–Colombian Oceanic Plateau. One Great Arc of the Caribbean (?). Geosphere 7, 468–493.
Yang, Y., Sahai, N., Romanek, C.S., Chakraborty, S., 2012. A computational study of Mg^{2+} dehydration in aqueous solution in the presence of HS^- and other monovalent anions — insights to dolomite formation. Geochim. Cosmochim. Acta 88, 77–87.
Zhang, F., Xu, H., Konishi, H., Kemp, J.M., Roden, E.E., Shen, Z., 2012. Dissolved sulfide-catalyzed precipitation of disordered dolomite: implications for the formation mechanism of sedimentary dolomite. Geochim. Cosmochim. Acta 97, 148–165.